Biochimica et Biophysica Acta 1838 (2014) 2053–2065

Contents lists available at ScienceDirect

Biochimica et Biophysica Acta

journal homepage: www.elsevier.com/locate/bbamem

Spectrum of Cav1.4 dysfunction in congenital stationary night blindness type 2☆

Verena Burtscher [a,1], Klaus Schicker [a,1], Elena Novikova [b], Birgit Pöhn [a], Thomas Stockner [c], Christof Kugler [a], Anamika Singh [d,2], Christina Zeitz [e,f,g], Marie-Elise Lancelot [e,f,g], Isabelle Audo [e,f,g,h,i], Bart Peter Leroy [j], Michael Freissmuth [c], Stefan Herzig [b], Jan Matthes [b], Alexandra Koschak [a,*]

[a] Medical University Vienna, Center for Physiology and Pharmacology, Department of Neurophysiology and -pharmacology, Schwarzspanierstrasse 17, 1090 Vienna, Austria
[b] University of Cologne, Department of Pharmacology and Center of Molecular Medicine, 50931 Cologne, Germany
[c] Medical University Vienna, Center for Physiology and Pharmacology, Department of Pharmacology, Währingerstrasse 13A, 1090 Wien, Austria
[d] University of Innsbruck, Institute of Pharmacy, Pharmacology and Toxicology, Center for Chemistry and Biomedicine, Innrain 80-82/III, 6020 Innsbruck, Austria
[e] INSERM, UMR_S968, Paris F-75012, France
[f] CNRS, UMR_7210, Paris F-75012, France
[g] UPMC Univ Paris 06, UMR_S 968, Institut de la Vision, Paris F-75012, France
[h] Centre Hospitalier National d'Ophtalmologie des Quinze-Vingts, INSERM-DHOS CIC 503, Paris F-75012, France
[i] UCL—Institute of Ophthalmology, 11–43 Bath Street, London EC1V 9EL, UK
[j] Dept of Ophthalmology & Center for Medical Genetics, Ghent University Hospital & Ghent University, 9000 Ghent, Belgium

ARTICLE INFO

Article history:
Received 12 February 2014
Received in revised form 11 April 2014
Accepted 23 April 2014
Available online 4 May 2014

Keywords:
L-type calcium channel
Cav1.4
Calcium channelopathy
Congenital stationary night blindness type 2

ABSTRACT

Defective retinal synaptic transmission in patients affected with congenital stationary night blindness type 2 (CSNB2) can result from different dysfunction phenotypes in Cav1.4 L-type calcium channels. Here we investigated two prototypical Cav1.4 variants from either end of the functional spectrum. Using whole-cell and single-channel patch-clamp techniques, we provide analysis of the biophysical characteristics of the point mutation L860P and the C-terminal truncating mutation R1827X. L860P showed a typical loss-of-function phenotype attributed to a reduced number of functional channels expressed at the plasma membrane as implied by gating current and non-stationary noise analyses. This phenotype can be rationalized, because the inserted proline is predicted to break an amphipatic helix close to the transmembrane segment IIIS1 and thus to reduce channel stability and promote misfolding. In fact, L860P was subject to an increased turnover. In contrast, R1827X displayed an apparent gain-of-function phenotype, i.e., due to a hyperpolarizing shift of the IV-curve and increased single-channel activity. However, truncation also resulted in the loss of functional C-terminal modulation and thus unmasked calcium-dependent inactivation. Thus R1827X failed to support continuous calcium influx. Current inactivation curtails the dynamic range of photoreceptors (e.g., when adapting to variation in illumination). Taken together, the analysis of two representative mutations that occur in CSNB2 patients revealed fundamental differences in the underlying defect. These may explain subtle variations in the clinical manifestation and must be taken into account, if channel function is to be restored by pharmacochaperones or related approaches.

1. Introduction

Several channel dysfunctions have been described that are caused by mutations in L-type calcium channel (LTCC) α1 subunits [1]. Mutations in the *CACNA1F* gene, which encodes Cav1.4 LTCC α1 subunits, have been associated with several X-linked visual disorders including Åland Island Eye Disease (AIED) [2], cone-rod dystrophy (CORDX3) [3], X-linked retinal disorder (XRD) [4], night blindness-associated transient tonic down-gaze (NATTD) [5] and incomplete congenital stationary night blindness (iCSNB, CSNB2) [6,7]. A majority of mutations identified was amongst patients that were originally diagnosed with CSNB2. Typical symptoms in CSNB2 are moderately low visual acuity,

☆ This work was supported by the Austrian Science Fund (FWF P-22528, SFB F44 (F4402) to AK), the Medical University Vienna and the foundations *Voir et Entendre* (CZ), Prix Dalloz for *"la recherche en ophtalmologie"* (CZ), Ville de Paris and Region Ile de France, and LABEX LIFESENSES [reference ANR-10-LABX-65] supported by French state funds managed by the ANR within the *Investissements d'Avenir programme* [ANR-11-IDEX-0004-0]. BPL is a Senior Clinical Investigator of the Research Foundation Flanders (Belgium) (FWO), and is further supported by FWO Flanders grant OZP 3G004306.

* Corresponding author at: Center for Physiology and Pharmacology, Department of Neurophysiology and -pharmacology, Medical University Vienna, Währingerstrasse 13a/Schwarzspanierstrasse 17, 1090 Vienna, Austria. Tel.: +43 1 40160 31220; fax: +43 1 4277 9641.
E-mail address: alexandra.koschak@meduniwien.ac.at (A. Koschak).
[1] These authors contributed equally to the work.
[2] Current address: Department of Biotechnology, Dr H. S. Gour University, Sagar, M.P 470003, India.

http://dx.doi.org/10.1016/j.bbamem.2014.04.023

myopia, nystagmus and variable levels of night blindness but one or more of these symptoms may be absent [6]. In addition, some patients report progressive photophobia. CSNB2 is therefore diagnosed on the basis of abnormalities in the human electroretinogram (ERG), which are compatible with a defect in neurotransmission within the retina between photoreceptors and second-order neurons. The typical Schubert–Bornschein ERG pattern of CSNB2 is one with an overall electronegative aspect, which was later further specified as the Miyake incomplete type [8,9].

Cav1.4 channels are predominantly expressed at release sites of mammalian photoreceptors in the outer plexiform layer of the retina. Cav1.4 dysfunction is therefore expected to change neurotransmitter release capacity and impair signalling to second-order retinal neurons. Many single point mutations have been functionally characterized. In the majority of the investigated mutants, channel activity was either abolished or dramatically reduced. It is not known whether the phenotype results from a decrease in protein expression, from reduced protein stability or from changes in the channel gating properties. Many Cav1.4 mutations are predicted to cause major structural changes, e.g. by truncation of the long C-terminus. Truncation of the C-terminus, however, does not necessarily result in misfolding of the channel. In fact, in many instances, truncated channels can still form functional channels.

Cav1.4 channels lack calcium-dependent inactivation due to active suppression by an inhibitory domain in their C-terminus [10,11]. This phenomenon is referred to as C-terminal modulation (CTM). It relies on the interaction between a distal and a proximal C-terminal modulatory domain [10]. In Cav1.4 (but also Cav1.3 and Cav1.2 [12,13]) channels, CTM determines not only CDI but also activation gating properties. Cav1.4 mutations with impaired CTM are of particular interest because (i) they display a gain-of-function due to a hyperpolarizing shift of the Cav1.4-mediated window current. (ii) In addition, these mutations reduce Ca^{2+} influx due to occurrence of CDI [11,12]. (iii) By analogy with recently published data on short Cav1.3 channels [12], enhanced open probability is predicted in truncated Cav1.4 channels. It is not clear, which of these processes dominates the phenotype of Cav1.4 mutants with impaired CTM function.

The ultimate goal is to remedy the deficits caused by the various mutations linked to CSNB2. This is contingent on mechanistic insights into the aberrations caused by the individual mutations. Here, we selected two mutations from either end of the spectrum: we report that the dysfunctional phenotype of point mutation L860P [14,15] was accounted for by a change in protein stability, which resulted in a drop in expression of functional channels. In contrast, in the C-terminal truncation mutant R1827X [15], C-terminal modulation was disrupted; this removed the break on calcium-dependent inactivation and thus resulted in transient calcium influx. In the absence of sustained Cav1.4-dependent calcium currents, photoreceptors are, however, predicted to be limited in their adaptation to different levels of illumination.

1.1. Experimental procedures

1.1.1. Cloning of mutant Cav1.4 channels

Both the CSNB2-associated point mutation Cav1.4 L860P [14,15] referred to as p.L849P in these publications and the truncation mutation Cav1.4 R1827X ([15]; referred to as p.R1816X therein) were introduced into the Cav1.4 α1 cDNA previously cloned from human retina (Genbank accession number, JF701915, length of open reading frame 5898 base pairs). Numbering of amino acids is according to the canonical reference sequence UNIPROT entry number: O60840-1. Numbering of the nucleotides (nt) in the constructs is given in parentheses. Mutants were constructed by applying standard geneSOEing technique. The mutation L860P was cloned in a two-step procedure, by replacing AgeI/ClaI (2069-3993) cassette obtained by SOE-PCR in an AgeI/ClaI (2069-3933)-cut Cav1.4 α1 construct in pBS. The mutated AgeI/EcoRI (2069-5027) cassette from L860P pBS was ligated into Age//EcoRI (2486-5444)-cut Cav1.4 α1 pCIneo construct. The mutation R1827X was constructed by inserting a stop codon at position nt 6542 by SOE-PCR. An EcoRI/NotI (5444-7225) cassette containing R1827X was ligated into the EcoRI/NotI (5444-7225)-cut Cav1.4 α1 pCIneo construct. A silent mutation for SmaI was introduced at nt position 6523 for identification. Regions subjected to PCR were confirmed by sequencing (MWG) in all expression constructs. Cloning of construct wild type Cav1.4 α1 in pCIneo has been described [16].

1.1.2. Cell culture and transfection

For whole-cell patch-clamp recordings, tsA-201 cells (ECACC, #96121229) were cultured in Dulbecco's modified Eagle's medium (DMEM, PAA, R15-801) supplemented with 10% fetal bovine serum (Gibco, 10270-106), 2 mM glutamine (Gibco, 25030-032) and maintained at 37 °C/10% CO_2. Cells were grown and split at 80% confluency using PBS-EDTA or trypsin for cell dissociation. Passage number did not exceed 30 passages. For whole-cell patch-clamp recordings tsA-201 cells were transiently transfected using ExGen500-invitro (Fermentas, R0511) according to the manufacturer's protocol or via calcium phosphate ($CaPO_4$) precipitation. For a 25 cm^2 flask with 30–40% confluency, 0.5 μg/2.25 μg (ExGen500-invitro/$CaPO_4$) of cDNA encoding the α1-subunits of either wt Cav1.4, R1827X or L860P were mixed with 0.5 μg/1.25 μg auxiliary $Ca_v\beta3$ and 0.5 μg/1.75 μg $Ca_v\alpha2\delta1$-subunits. $Cav1.3_{42}$ α1-subunit cDNA was used as control for gating current analyses (Genbank accession number: EU363339). A plasmid encoding EGFP (0.025–0.25 μg) was added to visualize successfully transfected cells. In some experiments, a plasmid (0.1 μg) was co-transfected that coded for the last 122 amino acids of Cav1.4 (C_{122}). Non-coding vector was added to keep the total DNA constant (4.5–7.5 μg). After overnight incubation with the transfection mixture cells were detached, replated on 35 mm cell culture dishes coated with poly-D-lysine and were kept at 30 °C/5% CO_2 prior to electrophysiological measurements (24–48 h). For single-channel recordings, HEK-293 cells were cultured in Petri dishes in Dulbecco's modified Eagle medium (DMEM, P010-11 0978, PAA, Austria) supplemented with 10% FBS (A15-151, Sigma, Deisenhofen, Germany), penicillin (10 units/ml), and streptomycin (10 μg/ml) (Sigma Aldrich). Cells were routinely passaged twice a week and incubated at 37 °C/6% CO_2. Cells were seeded onto 60 mm polystyrene Petri dishes (Falcon, Heidelberg, Germany) at a density of 1–2 × 10^4 cells/cm^2. The amount of wild type or R1827X α1-subunit, $Cav\beta_3$ and $Cav\alpha_1\delta$-1, GFP and pUC cDNA transfected was 0.5 μg, 0.5 μg, 0.5 μg and 0.5 μg and 3 μg, respectively. The cDNA mixture was delivered to the cells by Effectene® transfection (301425, Qiagen GmbH, Hilden, Germany) according to the manufacturer's guidelines. Sixteen to 20 h after transfection, cells were split and cultured in 35 mm polystyrene Petri dishes.

1.1.3. Immunoblotting

$CaPO_4$-transfection was employed to wild type and mutant Cav1.4 channels in tsA-201 cells as described above; for comparison mock transfections were done (α1 omitted; only β3, α2δ-1 and pUC). Membranes from transfected cells were prepared after homogenization in ice-cold lysis buffer: 10 mM Tris–HCl (pH 7.4) and protease mix: 0.2 mM PMSF, 0.5 mM benzamidine, 1 M pepstatin, 2 mM iodacetamide, 1 mg/ml leupeptin, 1 mg/ml aprotinin, and 100 mg/ml trypsin inhibitor. Immunoblotting was carried out as previously described [17]. Membranes (30 μg protein) were loaded onto an 8% SDS gel. Expression of recombinant subunits was monitored by blotting with α1 subunit-selective polyclonal sequence-directed antibodies (anti-calcium channel α1 subunit, pan antibody, C1103, Sigma Aldrich). Specific band sizes were observed at the expected molecular mass (in [kD]: wt, L860P: 220; R1827X: 203). For cycloheximide (CHX) chase experiments tsA-201 cells (confluency 70–80%, 175 cm^2 dish) were transfected with plasmids (3.5 μg each) encoding of α1 (wild type or L860P) in a 1:1:1 ration with Cavβ3 and Cavα2δ1-subunits using Turbofect (Thermo Scientific, R0531). In preliminary experiments the optimum conditions

were defined by applying CHX in different concentrations (3, 10 and 30 μM) for different periods (2, 4, 8 and 16 h). Finally cells were treated 42–44 h after transfection with 10 μM CHX for 2 and 4 h. Aliquots of the membranes (containing 30 μg protein) were loaded onto a 6% SDS gel (thickness: 1.5 mm). Immunoreactivity against Ponceau S staining served as loading control. We used Ponceau staining rather than any other housekeeping proteins, since the latter potentially also are degraded ([18]; also our observation). We therefore normalized the AUC of the intensity profile (ImageJ) of the immunoblot signal to the total protein signal (difference in protein load was <10%) revealed by Ponceau S staining.

1.1.4. Electrophysiological recordings

For *whole-cell patch-clamp recordings*, electrodes with a resistance of 2–5 MΩ were pulled from glass capillaries (borosilicate glass; 1.5 mm diameter, 0.32 mm wall thickness; Science Products) using a micropipette puller (P97, Sutter Instruments, USA) and fire-polished with an MF-830 microforge (Narishige, Japan). Cells were recorded in the whole-cell configuration using Axopatch 700B amplifier (Molecular Devices, USA). Data were analyzed using pClamp 10 software (Molecular Devices, USA). The pipette internal solution contained [in mM]: 135 CsCl, 10 HEPES, 10 EGTA, 1 $MgCl_2$ adjusted to pH 7.4 with CsOH (311 mOsm); bath solution [in mM]: 2–15 $CaCl_2$, ($BaCl_2$) 10 HEPES, 150 Choline-Cl, and 1 $MgCl_2$, adjusted to pH 7.4 with CsOH (320 mOsm). Current-voltage (*I–V*) relationships were obtained by holding cells at a potential of −98 mV (holding potential, HP) before applying 300-ms pulses to various test potentials. *I–V* curves were fitted to the equation $I = G_{max}\,(V - V_{rev})/\{1 + exp\,[(V_{0.5,act} - V)/k]\}$, where V_{rev} is the extrapolated reversal potential, *V* is the test potential, *I* is the peak current amplitude, G_{max} is the maximum slope conductance, $V_{0.5,act}$ is the half maximal activation voltage and *k* is the slope factor. The voltage-dependence of inactivation was assessed by applying a 50 ms test pulse to V_{max} before and after holding cells for 5 s at various conditioning test potentials. The (quasi) steady-state inactivation curves were analyzed using the following Boltzman relationship $I = I_{SS} + (1 - I_{SS})/(1 + \exp\,(V - V_{0.5,inact}/k_{inact}))$, where *I* is the peak current amplitude, I_{ss} is the non-inactivating fraction, *V* is the membrane potential, $V_{0.5,inact}$ is the half-inactivation potential, and k_{inact} is the slope factor. (±)-BayK8644 (Sigma Aldrich, B112, racemic) was dissolved in the external recording solution from a 10 mM stock solution in dimethyl sulfoxide (final concentration 0.1%) and perfused through a microcapillary onto cells using a pressure-driven (20–30 mmHg) perfusion system. Experiments showing currents bigger than 3 nA were prospectively excluded from analysis of activation and inactivation parameters to guarantee high-quality voltage-clamp. Ca^{2+}-dependent inactivation (CDI) was quantified as the current remaining at the end of 250 ms depolarisations to different test potentials (expressed as fraction of the peak current amplitude, r_{250}). Parameter *f* was defined as the maximal difference between r_{250} values of barium (I_{Ba}) and calcium (I_{Ca}) inward current observed within the investigated voltage range. ON-gating currents were digitized at 50 kHz and filtered at 4 kHz and quantified by current integration over the first 2.4–2.6 ms of the test pulse. The voltage dependence of Cav1.4 ON gating currents was determined by replacing the charge carrier with 15 mM Mg^{2+} supplemented with 15 μM $GdCl_3$ to maximally eliminate inward and outward current components. Cells were clamped to a holding potential of −98 mV and

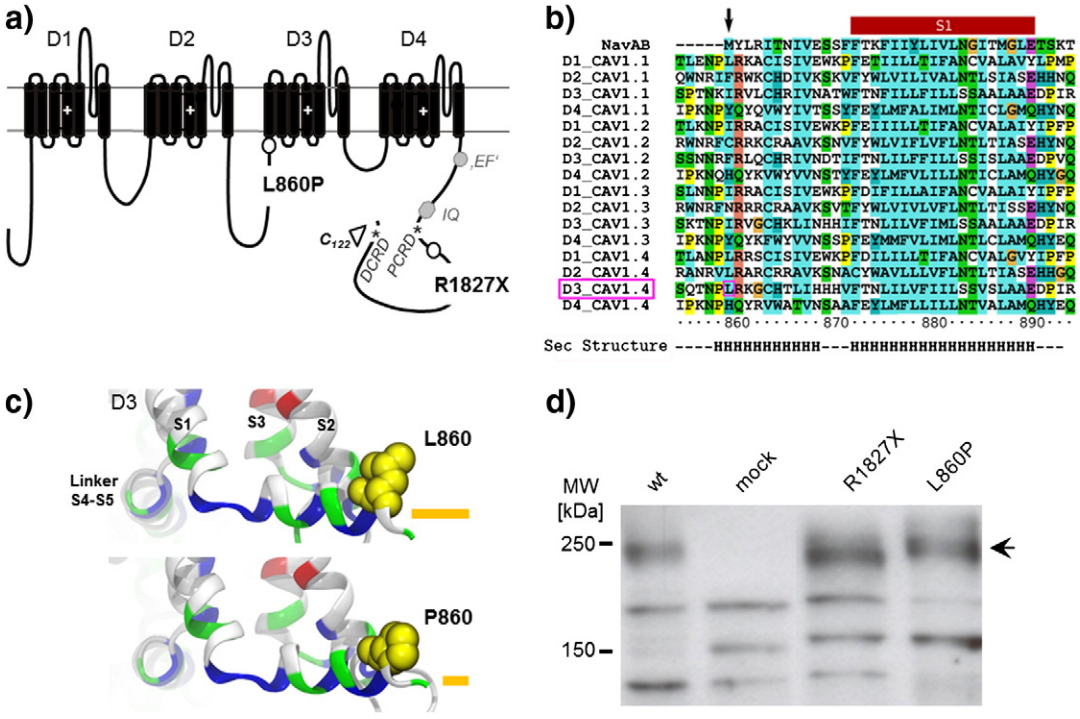

Fig. 1. Location and expression of Cav1.4 mutants L860P and R1827X. (a) Mutation L860P is located in the II–III loops whereas R1827X is a C-terminal truncation mutant. Their approximate position is shown in a transmembrane model of the Cav1.4 channel. Within the C-terminus, regulatory domains important for (voltage- and calcium-dependent) gating modulation have been depicted: the putative EF hand motif ('EF'), the IQ calmodulin binding motif (IQ) and the interacting domains for the C-terminal modulation (CTM): DCRD, distal regulatory domain; PCRD, proximal regulatory domain and C_{122}, the last 122 amino acid residues of the C-terminus. The length of the C-terminus comprising ~27% of the total protein is underestimated in this model figure. (b) Sequence alignment of amphipatic helix and helix S1 of the Cav1.x channels together with the sequence of the NavAB template and the secondary prediction of the Cav1.4 sequence. The prediction indicated that in Cav1.4 the amphipatic helix begins at position Pro859 and continues until residue His869. This helix is conserved between the NavAB template and the Cav1.x ion channels The S1 helix is indicated by a red bar, the position of the Leu860 in domain III (D3_Cav1.4) by the black arrow. (c) Homology model of Cav1.4: a zoom to the amphipatic helix close to the voltage sensor of the wild type (upper figure) and the L860P mutant (lower figure) is depicted. Residue 860 is shown in yellow space filling mode. Hydrophobic residues (white) are facing the membrane, whilst the polar (green) and charged (blue, positive/red, negative) residues are oriented towards the water phase of the cytosol. (d) Expression of wild type (wt) and mutant Cav1.4 α1 subunits in tsA-201 cells (+β3 + α2δ-1) was confirmed in Western Blot experiments (one out of 7 experiments is shown). The arrow marks the specific bands; theoretical molecular mass: 219 kDa for wild type and L860P, and 203 for R1827X. Mock, mock-transfected cells (β3 and α2δ-1 only).

depolarized to potentials in the range from −78 to +62 mV 10 mV increments for 10 ms. Capacitative transient currents were difficult to eliminate but they always showed a linear voltage-dependence (compared to the characteristic sigmoidal voltage-dependence of gating currents). We estimated the number of channels expressed in tsA-201 cell membranes by non-stationary noise analysis using the following protocol: cells were depolarized from a holding potential of −78 to +42 mV for 10 ms to maximally activate the channels before stepping back to −48 mV for 10 ms. The mean current and variance of 250–500 traces were calculated. To avoid interference with the capacitative transient we started the analysis shortly after the peak tail current reached its maximum (delay time: 5 × time constant of the voltage-clamp). To calculate the number of channels as well as the single channel current the following parabolic equation was used $\sigma^2 = i \cdot I - (I^2/N) + b$, where σ^2 is the variance of the mean tail current, i is the single channel current, I is the mean tail current, N is the number of channels and b is the background noise delineated by the variance offset [19]. The mean single channel current i is indicated by the initial slope of the curve and the interception point with the X-axis (I) represented the single channel current multiplied by the number of channels expressed (N) [$I = i \times N$] [19]. The number of channels per cell was normalized to the cell size assuming a specific capacitance of 1 μF/cm^2. All experiments shown were corrected for liquid junction potentials of −8 mV. A number of cells had to be excluded from the analysis because the data rather resembled a straight line than a parabola (which was the case when the maximum open probability was far below 0.5). The portion of excluded cells was higher in cells expressing L860P (33%) than wild type (25.7%).In *single-channel patch-clamp recordings* Cav1.4 single-channel currents in GFP-positive cells were recorded 48–72 h after transfection at room temperature (19–23 °C) as reported [12]. In brief, HEK-293 cells kept in 35 mm culture dishes were washed and placed in depolarizing bath solution containing [in mM]: 120 K-glutamate, 25 KCl, 2 $MgCl_2$, 10 HEPES, 2 EGTA, 1 $CaCl_2$, 1 Na_2-ATP, 10 dextrose (pH 7.4 with KOH). Patch pipettes made from borosilicate glass (1.7 mm diameter and 0.283 mm wall thickness, Hilgenberg GmbH, Malsfeld, Germany) were pulled using a Narishige PP-83 vertical puller and fire-polished using a Narishige MF-83 microforge (Narishige Scientific Instrument Lab, Tokyo, Japan). Pipettes showed typical resistances between 6 and 10 MΩ when filled with pipette solution [in mM]: 110 $BaCl_2$, 10 HEPES; pH 7.4 adjusted with TEA-OH. To enhance LTCC activity (S)-(−)-BayK 8644 (Tocris, 1546/10) was added to the pipette solution at a concentration of 10 μM. Single Ca^{2+}channels were recorded in the cell-attached configuration at test potentials ranging from −30 to 10 mV and depolarizing test pulses of 150 ms duration at 1.67 Hz (HP of −100 mV). Single-channel currents were filtered at 2 kHz, −3 dB, 4-pole Bessel, and sampled at 10 kHz with the Axopatch 1D amplifier using pClamp5.5 software (Molecular Devices, USA). The number of channels in a patch was estimated by the stacked openings observed. The channel events were detected using pClamp 6.0 software (Molecular Devices, USA), and Origin Pro 8 software (Microcal Software, Northampton, MA, USA) was employed for graphic analysis. Single-channel gating analysis was performed as described [21]. Note that data were not further filtered for analysis. Due to low activity at negative potentials unitary conductance of Cav1.4 channels was determined based upon amplitudes taken from well-resolved single-channel openings. Single-channel conductance was calculated as slope of the unitary current–voltage relationship.

1.1.5. Sequence alignments and homology modelling

Sequence alignment was done as previously described [20] using MUSCLE [21] and manually adjusted. Homology models were built using the Na_VAB crystal structure (PDB ID: 3RVY) [22] because the NavAB sodium channel is the most closely related ion channel for which a crystal structure has been determined. The NavAB sodium channel can serve as a template for L860P mutant, because Leu860 is still close enough to the S1 helix of the voltage sensor. For model building we applied MODELLER [23,24]. The best of 50 models, evaluated using the DOPE score [25] were selected for structural analysis.

1.1.6. Statistics

All values are presented as means ± S.E.M. for the indicated number of experiments (n). For multiple comparisons statistical significance was determined by Kruskal–Wallis test followed by Dunnett's post-hoc test. For comparisons of two groups, data were analyzed by Mann–Whitney *U*-test or by Wilcoxon signed-rank test as indicated for individual experiments. Statistical significance was set at $P < 0.05$.

2. Results

2.1. Characteristics and expression of two selected Cav1.4 mutants

A stop mutation in C-terminus at position Arg1827 (also p.Arg1816stop in [15]; Fig. 1a) was found in an 8-year old male patient from a Belgian family who presented with a classic CSNB2 phenotype. Full-field flash electroretinography (Suppl. Fig. 1) showed a pattern consistent with a Schubert–Bornschein, Miyake incomplete type of ERG [8,9]. The boy did not have any history of night blindness, but he suffered from photophobia from birth until he was 6 years old, without complaints of photophobia after that (for details see Supplemental

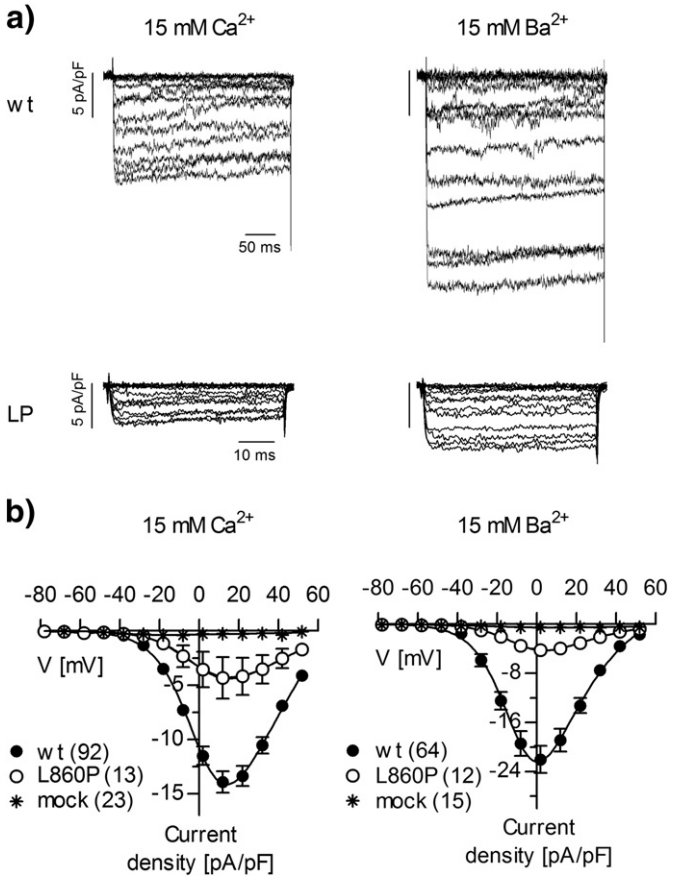

Fig. 2. Representative currents and current–voltage relationships of wild type and L860P channels. (a) Representative currents mediated by wild type (wt; upper panel, cells: 11511001.abf, 11421023.abf) and L860P (lower panel, cells: 11325001.abf, 11331007.abf; tsA-201 cells; +β3 and α2δ-1 subunits). 15 mM Ca^{2+} or Ba^{2+} was used as charge carrier. Cells were clamped to a holding potential of −98 mV and depolarized for 300 ms (wild type) or 50 ms (L860P) to potentials ranging from −78 mV to +52 mV (10 mV increments) every 5 s. (b) Current densities for wild type (black) and L860P (open circle) channels are depicted at different voltages for the charge carrier indicated. Asterisks, recordings form mock transfected cells. Data are shown as means ± SEM. Number of experiments is given in parentheses. For details and statistics see Table 1.

Table 1
Biophysical parameters and statistical comparison of wild type, R1827X and L860P channels using different charge carriers. Data are presented as means ± SEM. CD, current density; V_{rev}, reversal potential; $V_{0.5,\ act}$, half maximal voltage of activation, k_{act}, steepness of activation curve; G_{max}, maximum slope conductance; $V_{0.5,inact}$, half maximal voltage of inactivation, k_{inact}, steepness of inactivation curve; Max_{inact}, maximal inactivation observed at depolarized potential given in percent; ND, not determined. Statistics: we used the Kruskal Wallis test with Dunn's post hoc test for multiple comparisons.

	Wild type			R1827X				R1827X + C_{122}				L860P			
		SEM	N		SEM	N	p vs. wt		SEM	N	p vs. wt		SEM	N	p vs. wt
15 mM Ca^{2+}															
CD [pA/pF]	13.93	0.99	92	14.04	1.74	40	>0.05	10.91	1.56	18	>0.05	4.34	1.90	13	<0.001
V_{rev} [mV]	63.46	0.72	92	65.42	0.84	40	>0.05	66.61	2.34	18	>0.05	79.65	5.74	13	<0.01
$V_{0.5,act}$ [mV]	0.96	0.45	92	−12.78	0.42	40	<0.001	3.07	1.83	18	>.05	3.63	1.25	13	>0.05
k_{act} [mV]	9.60	0.12	92	8.50	0.14	40	<0.001	9.95	0.42	18	>0.05	12.61	1.11	13	<0.05
G_{max} [nS]	0.37	0.03	92	0.27	0.03	40	<0.05	0.30	0.05	18	>0.05	0.08	0.02	13	<0.001
$V_{0.5,inact}$ [mV]	−17.81	2.27	29	−29.56	1.09	30	<0.001	−18.83	6.58	5	>0.05	−12.83	1.61	4	>0.05
k_{inact} [mV]	−14.39	1.28	29	−8.35	0.49	30	<0.001	−8.25	1.43	5	>0.05	−13.79	2.06	4	>0.05
Max_{inact} [%]	91.71	1.98	29	82.87	2.04	30	<0.01	80.31	7.37	5	>0.05	88.84	5.40	4	>0.05
15 mM Ba^{2+}															
CD [pA/pF]	22.01	2.20	64	25.35	3.84	28	>0.05	6.95	0.58	10	<0.01	4.21	0.64	12	<0.001
V_{rev} [mV]	46.64	1.22	64	44.18	2.15	28	>0.05	51.34	3.84	10	>0.05	67.20	6.54	12	<0.001
$V_{0.5,act}$ [mV]	−9.46	0.58	64	−24.55	0.73	28	<0.001	−3.57	1.89	10	>0.05	−11.05	1.50	12	>0.05
k_{act} [mV]	8.7	0.11	64	6.14	0.23	28	<0.001	9.58	0.49	10	>0.05	9.04	0.74	12	>0.05
G_{max} [nS]	0.65	0.07	64	0.54	0.09	28	>0.05	0.19	0.03	10	<0.01	0.09	0.02	12	<0.001
$V_{0.5,inact}$ [mV]	−26.59	2.02	19	−29.46	2.57	13	>0.05	ND	ND	ND	ND	−33.46	2.41	4	>0.05
k_{inact} [mV]	−10.33	0.66	19	−12.31	1.99	13	>0.05	ND	ND	ND	ND	−11.55	2.58	4	>0.05
Max_{inact} [%]	84.94	2.94	19	76.12	3.47	13	>0.05	ND	ND	ND	ND	98.09	1.10	4	<0.05
2 mM Ca^{2+}															
CD [pA/pF]	4.48	0.47	11	8.14	1.47	19	>0.05	4.30	0.53	9	>0.05	ND	*ND*	*ND*	*ND*
V_{rev} [mV]	*60.52*	*3.02*	*11*	*64.79*	*4.31*	*19*	*>0.05*	*62.04*	*4.72*	*9*	*>0.05*	*ND*	*ND*	*ND*	*ND*
$V_{0.5,act}$ [mV]	*−22.40*	*1.42*	*11*	*−29.41*	*1.84*	*19*	*>0.05*	*−10.79*	3.69	9	>0.05	ND	ND	ND	ND
k_{act} [mV]	7.56	0.51	11	6.97	0.27	19	>0.05	9.66	0.64	9	>0.05	ND	ND	ND	ND
G_{max} [nS]	0.08	0.01	11	0.17	0.03	19	>0.05	0.18	0.07	9	>0.05	ND	*ND*	*ND*	*ND*

information). This C-terminal mutation is particularly interesting because the proximal regulatory domain important for CTM of Cav1.4 is still present in R1827X channels. This is in contrast to a previously published truncation mutant [10] and provided us with the opportunity to test, if complementation with the missing C-terminal fragment functionally rescues the R1827X mutant (see below).

We selected a second mutation, where a proline residue replaced Leu860 (p.Leu849Pro in [14,15]). The L860P mutation is located in the loop between transmembrane domains II and III in a conserved amphipatic helix (Fig. 1b), which runs in parallel to the membrane plane and precedes the S1-helix of transmembrane domain III (Fig. 1c). As shown in Fig. 1c, position 860 is on the membrane-facing side of the amphipatic helix. As indicated in Fig. 1b, the helix begins at position 859 with another proline, which is a frequent helix capping residue. The subsequent second proline, however, shows strong helix breaking properties because it lacks the amide hydrogen necessary for helical hydrogen bond formation. In wild type Cav1.4, the hydrophobic side chain of Leu860 is predicted to extend into the hydrophobic core of the membrane (Fig. 1c). Moreover, the proline mutation changes the long hydrophobic residues Leu into a compact hydrophobic residue (Fig. 1d).

These two prototypical Cav1.4 mutants were heterologously expressed in tsA-201 cells and the presence of the proteins confirmed by immunoblotting (Fig. 1e).

2.2. Functional expression of mutant L860P channels

The model depicted in Fig. 1 predicts that the substitution of Leu860 by proline impairs the folding of the mutant ion channel. Impaired folding of membrane protein results in its retention in the endoplasmic

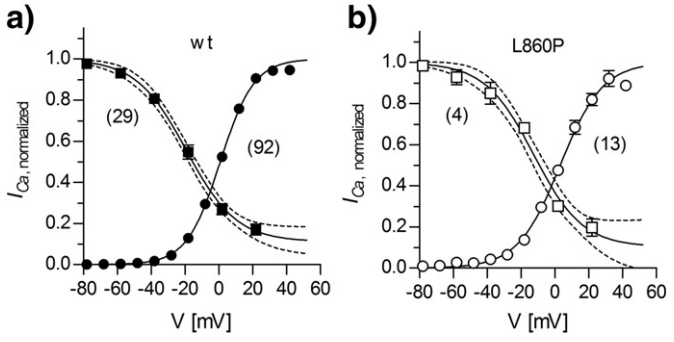

Fig. 3. Voltage-dependent activation and inactivation properties of wild type and L860P channels using 15 mM Ca^{2+} as charge carrier. Calculated fit parameters in [mV]: $V_{0.5,act}$: wild type (wt): 1.0 ± 0.5, L860P: 3.6 ± 1.3; k_{act}: wild type: 9.6 ± 0.12, L860P: 12.6 ± 1.11*; $V_{0.5,inact}$: wild type: −17.8 ± 2.3, L860P: −12.8 ± 1.6; k_{inact}: wild type: −14.4 ± 1.3, L860P: −13.8 ± 2.1. *, $p < 0.05$; ***, $p < 0.001$. Colour code for wild type (a) and L860P (b) is as in Fig. 2. The dotted lines indicate the 95% confidence interval of the fit. Data are presented as means ± SEM for the indicated number of experiments.

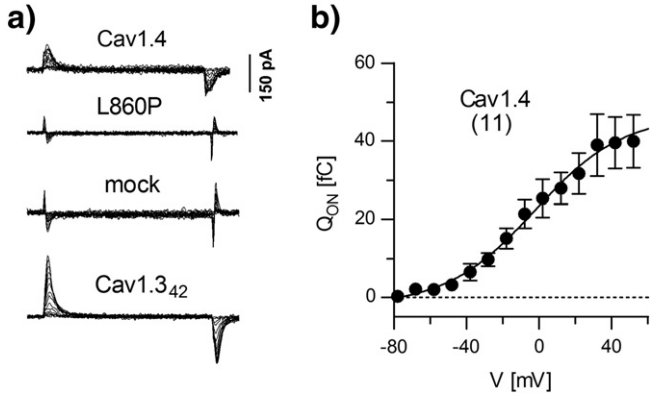

Fig. 4. Gating current properties of wild type and L860P channels. (a) Representative traces showing gating currents for Cav1.4 wild type (wt) and L860P channels. We never detected a distinct gating current for L860P channels. Mock-transfected cells were used as negative and $Cav1.3_{42}$-transfected as positive control. (b) Voltage-dependence of integrated ON-gating currents was recorded in the presence of 15 mM Mg^{2+} and 15 μM Gd^{3+}. Parameters describing the Q_{ON}–voltage relationship for wild type Cav1.4: $V_{0.5}$: −4.0 ± 4.0 mV, k: 23.1 ± 1.8, n = 11.

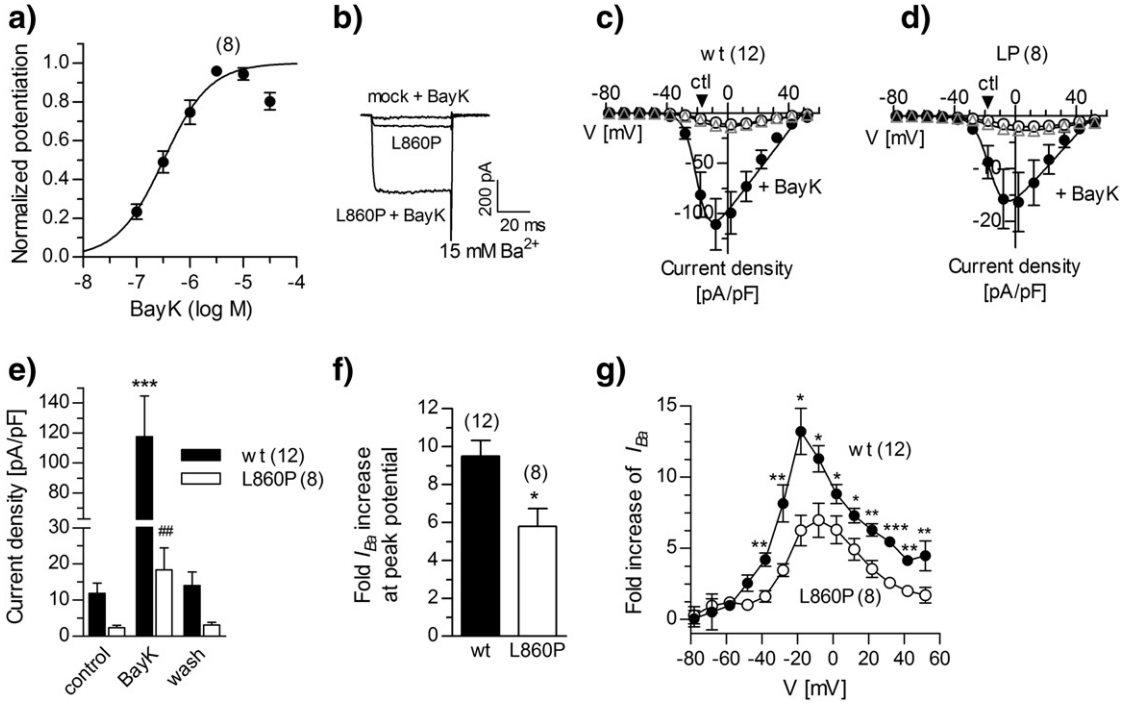

Fig. 5. Potentiation of current amplitude of wild type and L860P channels by the LTCC activator BayK 8644. (a) BayK concentration-response relationship for wild type I_{Ba} potentiation. The solid line indicates a nonlinear fit to the data ($logEC_{50}$ [M] = −6.49 ± −0.05; EC_{50} = 0.8 μM). The data point observed for the highest concentration was excluded for the fit analysis because we used a racemic mixture showing antagonistic properties at high concentrations. (b) Representative traces of maximal I_{Ba} for L860P ± BayK compared to mock + BayK; 3 μM (c, d) Effect of 3 μM BayK on the current density of wild type (wt, c) or L860P channel expressing cells (d) at different voltages. BayK was completely washed out after each application (grey up-triangle). Ctl, without BayK. (e) Effect of BayK on the maximal current density of wild type and L860P. Friedman-test with Dunn's post hoc test was used for multiple comparisons: ***, $p < 0.001$, ##, $p < 0.01$ versus respective control. (f) Fold-increase of peak current density in the presence of BayK for wild type (black) and L860P (grey) currents. (g) Extent of potentiation of current density of wild type or L860P channels observed at various voltages. *, $p < 0.05$, **, $p < 0.01$, ***, $p < 0.001$; Mann Whitney *U*-test.

reticulum. Accordingly, we anticipated a reduction in channel density of L860P. This was indeed observed: whole-cell patch-clamp recordings showed a significant reduction in current density for L860P compared to wild type irrespective of whether Ca^{2+} (Fig. 2, left) or Ba^{2+} (Fig. 2, right) was used as the charge carrier (see also Table 1). Recordable L860P currents differed from those found in mock-transfected (β_3/$\alpha_2\delta$-1) cells which mediated no detectable voltage-dependent inward currents (Fig. 2). Small sized L860P currents (15 mM Ca^{2+}: 4 versus 14 pA/pF in wild type t; Table 1) did not allow us to perform reliable experiments at lower (i.e. more physiological) Ca^{2+} concentrations. However, both activation (Figs. 2, 3) and inactivation (Fig. 3) gating properties were comparable to that of wild type currents (see also Table 1).

Reduced current density can be attributed to a decline in the number of channels expressed in the plasma membrane. Alternatively, it may also arise from changes in the single channel properties. Immunoblots were performed with membrane fractions prepared by differential centrifugation. The endoplasmic reticulum represents the bulk of these membranes, whilst the plasma membranes are only a minor fraction of the total membranes. Hence, it is not possible to deduce the level of surface expressed channels from the immunostaining intensity, although there was a trend consistent with reduced expression of L860P

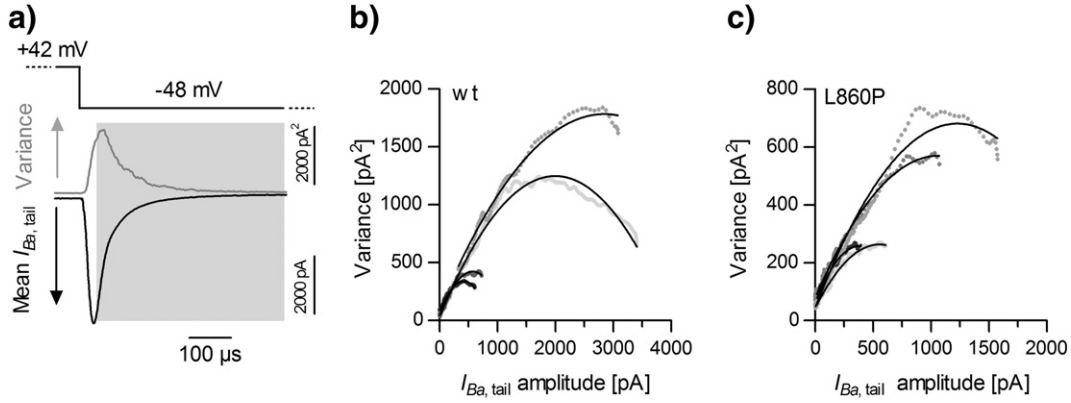

Fig. 6. Channel number estimation for wild type and L860P investigating non-stationary noise analysis (a) Cells were depolarized from a holding potential of −98 mV to +42 mV for 10 ms (to maximally activate Cav1.4 channels) before stepping back to −48 mV for 10 ms (a potential at which Cav1.4 channel are still closed; 15 mM Ba^{2+}, see Figs. 2b and 5c, d). Mean tail current and variance were calculated from 250 to 500 traces within the shaded area. (b, c) Exemplar variance versus mean current amplitude plots for cells expressing wild type (wt; in b; cells: 12n12019.abf, 12n28006.abf, 12n29018.abf, 12d01001.abf) or L860P (in c, cells: 12n14039.abf, 12n23024.abf, 12n23030.abf, 12n27030.abf) channels. Solid lines represent the parabolic data fit. The initial slope gave the mean single channel current *i*, and the interception point with the X-axis (*I*) represented the single channel current multiplied by the number of channels expressed (*N*) [$I = i \times N$].

(3 out of 7 experiments showed a clear-cut reduction). Thus, we addressed this question by approaches that relied on recording functional channels: a reduction in the nonlinear gating charge movement (gating currents, [26]) indicates a decrease in the number of channels capable of undergoing voltage-dependent gating. Hence, it is a direct proof for a lower number of Cav1.4 channels at the plasma membrane. We measured gating currents by replacing the Ca^{2+} or Ba^{2+} with an equimolar concentration of Mg^{2+} in the bath solution supplemented with the pore-blocking cation Gd^{3+} (15 μM) to entirely block inward currents and minimize outward currents. Wild type Cav1.4 gating currents were clearly visible (Fig. 4a, top trace; n = 11) and showed typical sigmoidal voltage-dependent behaviour (Fig. 4b). In contrast, we never observed distinct gating currents for L860P (n = 4) (Fig. 4a, second trace; n = 4). Rather, recordings were comparable to those obtained in mock-transfected $\beta_3/\alpha_2\delta$-1 cells (Fig. 4a, third trace, n = 6).

We further corroborate this finding by non-stationary noise analysis (NSNA). This provided an estimate of the number of channels per transfected tsA-201 cell. We conducted NSNA in the presence of 3 μM of the LTCC activator BayK8644 to increase the mean open time and thus allow for more sensitive data analysis (Fig. 5). This concentration caused maximum activation of wild type Cav1.4 (Fig. 5a). BayK8644 also clearly augmented currents through Cav1.4 wild type and L860P channels, but it did not have any detectable effect in mock-transfected cells (Fig. 5b).

Tail currents reflect the sequential closure of individual channels; the actual current is the sum of currents through individual channels that are still open. To exclude potential differences in the intrinsic closing rate of the channels we calculated the kinetics of deactivation which were not significantly different between wild type and L860P (tail current decay: τ [ms]: wild type: 0.17 ± 0.03, n = 8; L860P 0.15 ± 0.03, n = 9; p > 0.05, Mann–Whitney *U*-test (in the presence of 15 mM Ba^{2+} and 5 μM BayK). Fluctuations (non-stationary noise) are caused by opening and closing of ion channels. Hence, there is no (or low) noise, if all of the channels are permanently closed, because the probability of finding the channel open, *Po* is (close to) zero. The same is true, if all channels are permanently open (*Po* = 1). Accordingly, the variance of the current, (pA^2, i.e., the sum of squared deviations from the mean) will be small (Fig. 6a). Fluctuations (variance) will be highest when *Po* is around 0.5. The plot of the trial-to-trial variance against current amplitude at different time points was best fitted with a parabolic function (Fig. 6 b, c). We concluded from our experiments that the number of wild type and L860P channels was generally low with a tendency to less expression of mutant L860P channels (channels/μm^2 for wild type: 2.5 ± 0.3, n = 27 and L860P: 1.9 ± 0.3, n = 14; p = 0.13, Mann Whitney *U*-test).

Under our strong depolarizing conditions (+42 mV) used in NSNA we could also estimate the maximal *Po* which was similar in wild type and L860P (wild type: 0.63 ± 0.02, n = 26; L860P: 0.61 ±0.03, n = 14; p = 0.4, Mann–Whitney *U*-test). These analyses do not rule out an effect of the L860P mutation on single channel activity of Cav1.4 at physiologically more relevant lower potentials.

2.3. Loss-of-function phenotype of mutant L860P channels

Considering the study by Doering and colleagues, activity of single Cav1.4 channels is expected to be quite low [27]. Nevertheless, it was possible to perform single channel analyses in wild type and mutant Cav1.4 channels (see also Fig. 11). We increased the fraction of sweeps with active channels by recording I_{Ba} (110 mM charge carrier) in the presence of 10 μM BayK8644 in the pipette solution. At a potential of −20 mV the number of active sweeps was slightly higher in L860P than in wild type (f_{active} [%]: wild type: 2.5 ± 0.4, n = 5; L860P: 9.8 ± 2.9, n = 5; p < 0.05) as was the *Po* (in [%]: wild type: 0.058 ± 0.009, n = 5; L860P: 0.14 ± 0.082, n = 5; p < 0.05). However, these effects were not seen at higher potentials (−10 and 0 mV) and do therefore not indicate a left shift in activation. These findings are in line with our whole-cell patch-clamp experiments. We observed apparent openings with the amplitude slightly above baseline noise that we did not identify as Cav1.4 channel activity because such events were also detected in untransfected cells (not shown). Although we did not find a significant difference in the mean open time (in [ms] wild type: 0.39 ± 0.03, L860P: 0.4 ± 0.03) we cannot rule out that such apparent openings interfered to a minor extent with our analyses.

We further determined the stability of L860P in a CHX chase experiment. CHX blocks the translocation step in elongation and therefore inhibits protein synthesis [28]. The model outlined in Fig. 1c predicts that L860P protein is less stable than the wild type because of destabilization of the amphipatic helix by P860. This conjecture was verified by examining the fate of newly synthesized L860P protein after addition of CHX. A representative immunoblot is shown in Fig. 7: the levels of wild type Cav1.4 remained essentially constant over the first 4 h-period after the CHX block had been imposed. In contrast, L860P already started to decrease after 2 h. This was seen in 5 out of 5 experiments with L860P.

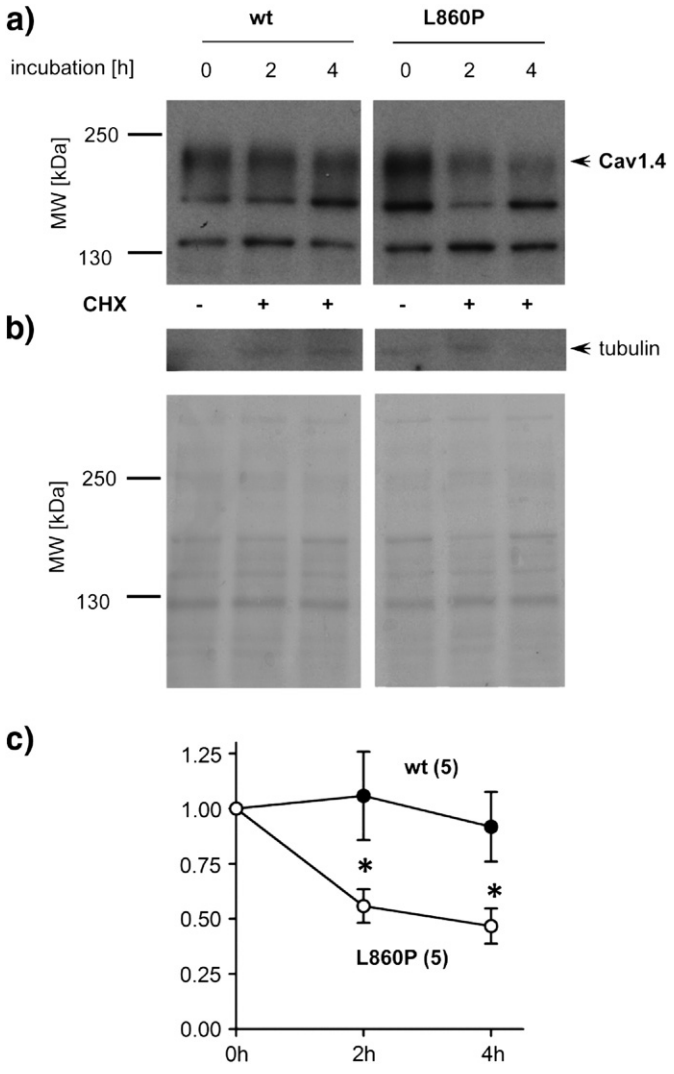

Fig. 7. Degradation of wild type and L860P channels. Transfected tsA-201 cells for CHX chase experiments were processed as described in Experimental procedures. (a) Total protein was prepared at time point 0 and after 2 and 4 h of exposure to CHX (10 μM). One out of 5 experiments is depicted for both wild type (wt) and L860P. L860P protein was degraded more rapidly than wild type, a characteristic of destabilized, misfolded protein. (b) Immunoreactivity against Ponceau S staining served as loading control. We also investigated an anti- β-tubulin antibody (shown above) (c) Protein stability normalized to total protein signal revealed by Ponceau S staining. L860P protein was degraded more rapidly than wild type, a characteristic of destabilized, misfolded protein. *, p < 0.05, two-way Anova with Bonferroni post test. Data are presented as means ± SEM for the indicated number of experiments.

For wild type, we did not observe any appreciable reduction in three experiments, but in two experiments the decrease in protein level was similar to L860P. While we do not understand the source of the variability in the case of wild type Cav1.4, these findings indicate that the proline insertion leads to higher Cav1.4 protein turnover in transfected tsA-201 cells.

Taken together, the observations are consistent with a model, where the reduced functional activity of L860P channels arises from a reduction in protein stability (and therefore fewer channels in the membrane) rather than any major additional change in channel gating.

2.4. Functional expression of mutant R1827X channels

We monitored expression of R1827X channels by recording their voltage- and time-dependent properties (15 mM or 2.5 Ca^{2+} and 15 mM Ba^{2+}; Fig. 8a, Table 1). Under physiological Ca^{2+} concentrations (2 mM), currents through wild type channels activated at negative potentials (5% current activation at -29.2 ± 0.7 mV). R1827X channels showed a shift in the voltage-dependence of activation to more negative voltages (seen in all recording conditions Fig. 8b, Table 1), typical for Cav1.4 channels lacking CTM [10]. The voltage-dependence of inactivation was also shifted to negative potentials in 15 mM Ca^{2+} resulting in a negative shift of the window current (Fig. 8c, Table 1).

As expected, I_{Ba} inactivation was slow in wild type Cav1.4; this voltage-dependent inactivation was even slower in R1827X during the 5 s depolarizing pulses (Fig. 9a, b). We compared the maximal inactivation of I_{Ba} observed with the (quasi) steady-state protocol (Fig. 8c) with the corresponding I_{Ba} inactivation during a test pulse to the voltage of maximal current influx (V_{max}) (Fig. 9a, b): we noticed that these data were not consistent. In the steady state protocol maximal inactivation was about 92 and 83%, whereas in the 'V_{max}' protocol we observed 76 ± 5.4% and 49.4 ± 5.3% inactivation for wild type (n = 12) and R1827X (n = 5), respectively. This difference can either be attributed to run down during the long-lasting experiment [29] or may result from a slow recovery from the inactivated state. As seen in Fig. 9c and d, recovery from I_{Ba} inactivation was indeed very slow (~120 s) and was twice as long as the inter-sweep interval in our steady state protocol. We therefore assume that the observed difference is accounted for by accumulation of the channel in the inactivated state. A comparison of wild type and R1827X showed a similar mono-exponential time course of recovery from inactivation (Fig. 9d). Recovery was complete for R1827X (105.1 ± 6.0%). The current amplitude measured for wild type Cav1.4 reached about 90% of the control current amplitude. Maximum recovery of wild type Cav1.4 was estimated from the fitted curves and was found to be variable, but it did not differ significantly from 100% ($p > 0.05$, Wilcoxon signed-rank test, n = 9).

In the presence of calcium, currents through R1827X channels decayed in a manner consistent with the absence of CTM: I_{Ca} through Cav1.4 R1827X inactivated rapidly (cf. traces recorded in the presence

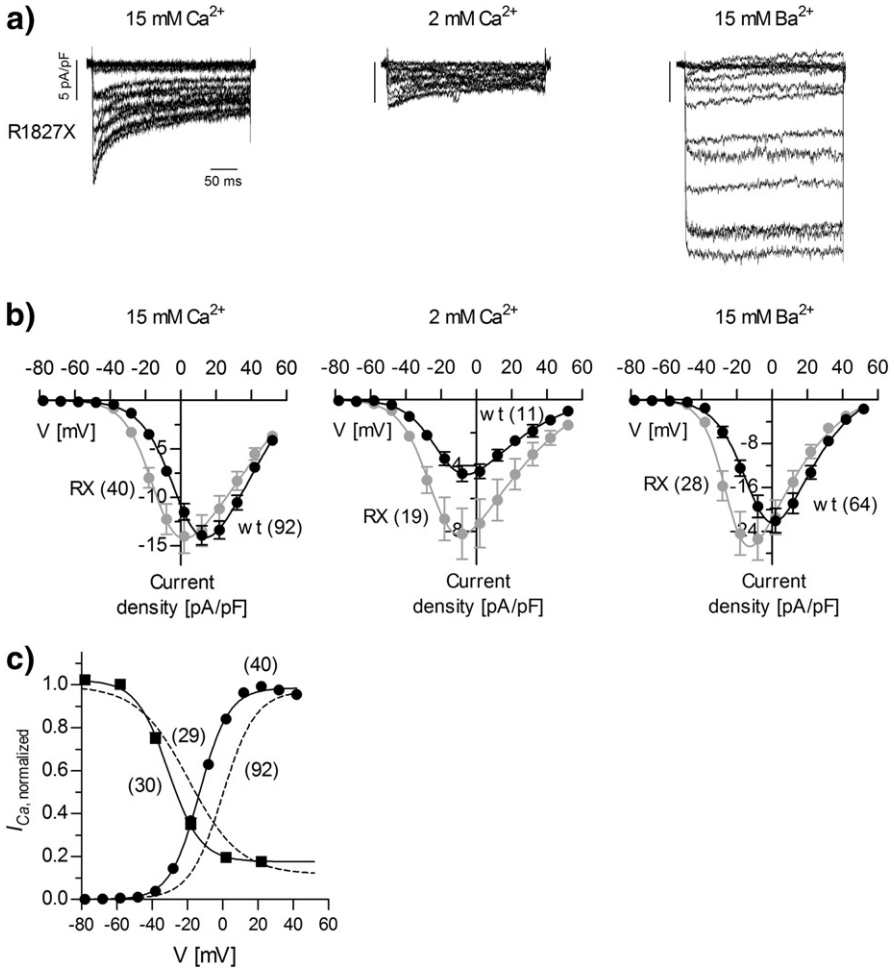

Fig. 8. Representative currents and gating properties of wild type and R1827X channels. (a) Representative currents mediated by mutant R1827X channels (cells: 11006042.abf, 12206004.abf, 11407026.abf; tsA-201 cells: +β3 and α2δ-1 subunits). (b) Current densities for wild type (wt) or R1827X channels are depicted at different voltages for the charge carrier indicated. Data are shown as means ± SEM. Number of experiments is given in parentheses. For details see Table 1. (c) Voltage-dependent activation and inactivation properties of R1827X using 15 mM Ca^{2+}. Calculated fit parameters in [mV]: $V_{0.5,act}$: $-12.8 \pm 0.4^{***}$; k_{act}: 8.5 ± 0.14; $V_{0.5,inact}$: $-29.6 \pm 1.1^{***}$; k_{inact}: -8.4 ± 0.5. ***, $p < 0.001$. The dotted lines show the data fit for wild type taken from Fig. 3 as a comparison. Data are presented as means ± SEM for the indicated number of experiments.

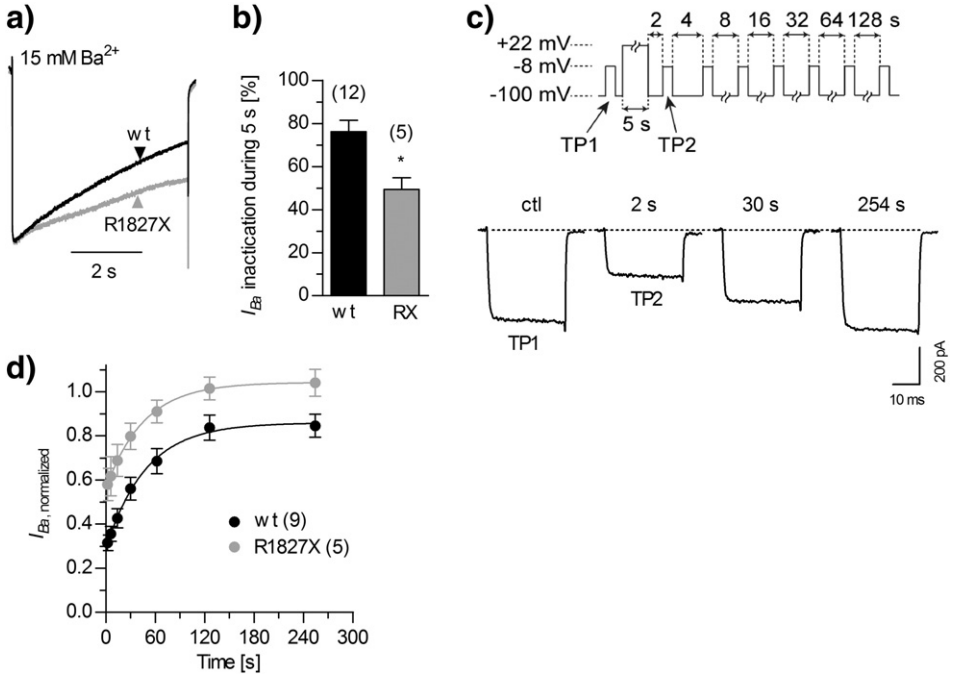

Fig. 9. Inactivation and recovery properties of in wild type and R1827X channels. (a) Inactivation sample traces recorded from cells expressing either wild type (wt) or R1827X channels during a 5 s inactivating test pulse to V_{max} (cells: 11325001.abf; 11331007.abf for wild type and R1827X). (b) Extent of inactivation during the 5 s test pulse. Percent of inactivation was 76.1 ± 5.4, n = 12 and 49.4 ± 5.3*, n = 5 for wild type and R1827X, respectively; *, $p < 0.05$, Mann–Whitney *U*-test (c) Upper panel: protocol to elicit recovery from inactivation: cells were depolarized to +2 mV for 50 ms (TP1; ctl, control) followed by an inactivating prepulse to +22 mV for 5 s and allowed to recover at a holding potential of −98 mV for the indicated time before a second TP was applied (+2 mV, 50 ms; TP2). Lower panel: representative experiment for wild type channel during TP1 and TP2 at different time points. (d) Recovery curves for wild type or R1827X using 15 mM Ba^{2+} as charge carrier. Currents elicited during TP2 were normalized to the TP1 current amplitude. Data were best fitted with a mono-exponential function (solid line) yielding time constants τ [in ms] 55.9 ± 11.1 and 45.9 ± 8.6 for wild type and R1827X, respectively ($p > 0.05$, Mann–Whitney *U*-test). Total recovery was 87.5 ± 5.4 and 105.1 ± 6.04% for wild type and R1827X respectively. No significant difference from 100% was observed; $p > 0.05$, Wilcoxon signed-rank test.

of equimolar Ca^{2+} and Ba^{2+} in Fig. 8a) and was subject to pronounced calcium-dependent inactivation (cf. Fig. 10b, d).

Differences between R1827X and wild type Cav1.4 channels may arise from changes in the gating mechanism. We previously showed that short forms of Cav1.3 channels had a much higher *Po* than long Cav1.3 channels [13]. It is evident that there is an analogy with R1827X, which is a short version of wild type Cav1.4. Therefore we analyzed single channel activity of R1827X channels using 110 mM Ba^{2+} as charge carrier. In the presence of 10 μM BayK8644, single-channel activity of wild type Cav1.4 steeply increased from 0.6 ± 0.1% at −20 mV (n = 5) to 5.0 ± 1.2% at +10 mV (n = 2). This indicates that the potentials applied were within the range of the activation threshold. As can be seen from representative traces depicted in Fig. 11a, the activity of single channel activity of R1827X was significantly higher than that of wild type. This was not due to a change in the open times (Fig. 11c) but to an increase in the open probability: at any given test potential the *Po* of R1827X was higher that of wild type channels (Fig. 11d). These data are consistent with the leftward shift of current-voltage curve for R1827X observed in whole-cell recordings (cf. grey curves in Fig. 8b). Based on the amplitudes of single openings we calculated a unitary conductance that was similar for wild type and R1827X channels (8.9 ± 1.0 and 10.9 ± 0.5 pS, n = 4 and 5, respectively; $p > 0.05$; Fig. 11e). The difference in the unitary conductance of wild type channels compared to data by Doering and colleagues (~4pS, [27]) is likely explained by the different analytic approach and the use of additional filtering in their study.

2.5. Loss-of-function phenotype of mutant R1827X channels

It is difficult to classify R1827X channels because they show an apparent gain-of function due to a hyperpolarizing shift of the window current (Fig. 8c), which is likely due to the increase in *Po* (Fig, 11d). Concomitantly, they display a loss-of-function due to calcium-dependent inactivation, which reduces Ca^{2+} influx (Figs. 8a and 10b, d). The experiments presented so far did not address the question, which of these changes in channel function were of pathophysiological relevance. When we calculated the charge transfer during 300 ms test pulses to various potentials (2 mM Ca^{2+}, Fig. 10f), we did not find any significant difference between wild type and R1827X in the physiologically relevant voltage range (−55 to −35 mV). However, we observed a frequency-dependent decrease in the charge transfer when we applied 20 ms depolarizing pulses to −20 mV (corresponding to −42.4 mV and −36.6 mV for wild type and R1827X channels, respectively; 2 mM Ca^{2+}) at frequencies of 1, 2 and 5 Hz (Fig. 12a) from a holding potential of −70 mV. These experiments were done in the presence of 3 μM BayK8644 and 15 mM Ca^{2+} as charge carriers because otherwise Cav1.4 currents were too small at the given voltages. Ca^{2+} influx through wild type Cav1.4 remained constant irrespective of frequency (Fig. 12b, c). In contrast, Ca^{2+} entry through R1827X channels was progressively decreased at 2 and 5 Hz (Fig. 12b, d). This finding must result from calcium-dependent inactivation. This interpretation was substantiated by examining the gain-of-function mutation I745T ([30], which shows a −30 mV shift in the voltage dependence of activation [29]; also our observation, not shown). Under the conditions employed in Fig. 12, I745T was indistinguishable from wild type (n = 4 − 6). This protocol was designed to mimic conditions of light illumination (at the holding potential) with short periods of darkness (during the test pulse); 5 Hz is a low frequency used to assess the flicker fusion frequency under conditions for scotopic rod vision [31]. We therefore conclude that, under physiological conditions, truncation of the C-terminus of Cav1.4 results in a loss of function because the truncated channels are incapable of supporting continuous calcium influx during changes in illumination. Usually this is preserved by the

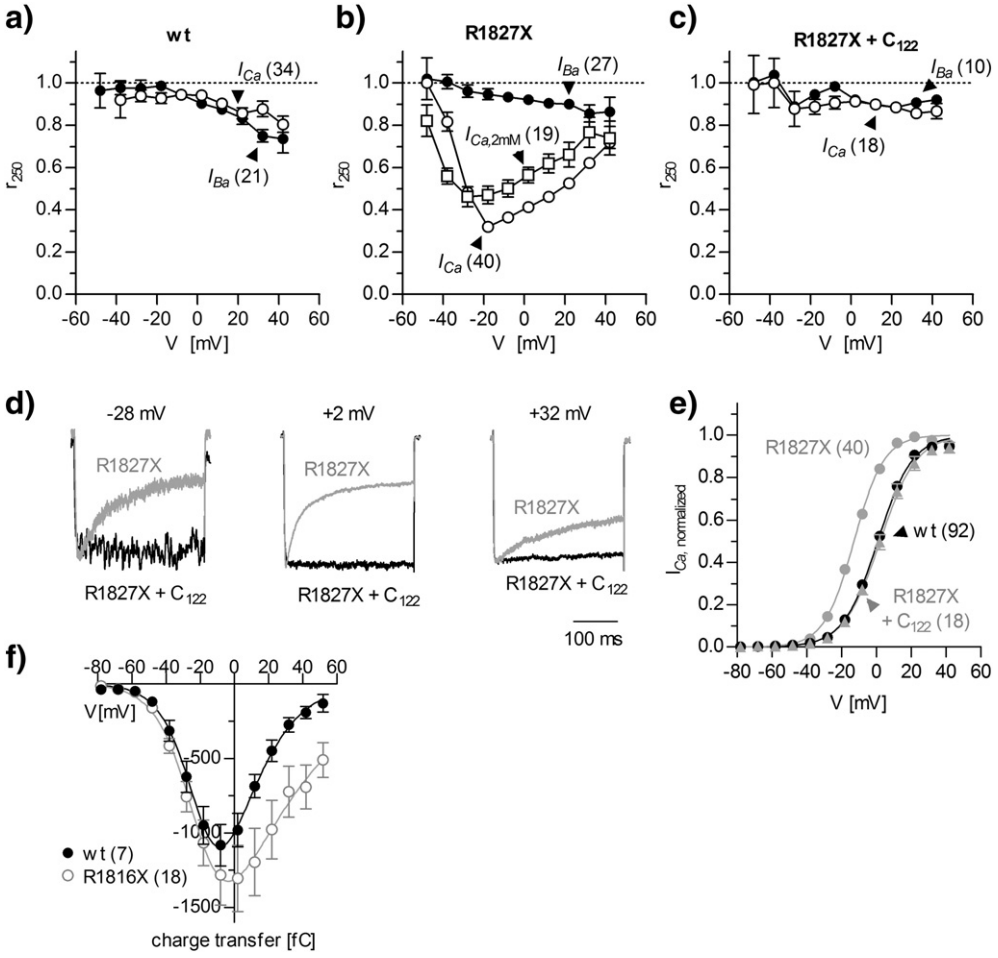

Fig. 10. Calcium-dependent gating properties of R1827X channels and its functional rescue. (a, b) Comparison of the r_{250} values (ratio between peak current and current after 250-ms of depolarization) at the indicated potential using either 15 mM Ba^{2+} (filled circles), 15 mM Ca^{2+} (open circles) or 2 mM Ca^{2+} (open squares) as charge carrier for (a) wild type (wt) and (b) R1827X. (c) Comparison of the r_{250} values in cells expressing R1827X together with the GFP-tagged C-terminal fragment Cav1.4-C_{122} (C_{122}; corresponding to the last 122 amino acids of the Cav1.4 C-terminus). (d) Normalized representative currents for R1827X alone (+β3 + α2δ-1) (grey; cell: 12426012.abf) or together with C_{122} (black; cell: 11915028.abf). Cells were depolarized to the potentials indicated. (e) Activation curves of wild type (black circles), R1827X alone (grey circles) or R1827X + C_{122} (up-triangle). Data are presented as means ± SEM. Number of experiments is indicated in parentheses. For statistical comparison of parameters see Table 1. (f) Integrated currents corresponding to the area under normalized I_{Ca} (transfer of charge Q) during 300 ms pulses to various test potentials are shown for wild type and R1827X channels compared at different voltages using 2 mM Ca^{2+} as charge carrier. No difference in the charge transfer between wild type and R1827X was observed in the voltage range physiologically relevant for photoreceptor function (−55 to −35 mV). Number of experiments performed is given in parentheses.

non-inactivating nature of Cav1.4 channels; a peculiarity amongst the family of LTCCs likely to be explained the very slow entry of Cav1.4 channels to the closed-state inactivation Cav1.4 (Suppl. Fig. 2 and Suppl. Table); in comparison to Cav1.2 [32].

2.6. Rescue of mutant R1827X channels

The experiments summarized above were designed to provide mechanistic insights into the dysfunction underlying two representative Cav1.4 channelopathies. The acid test for a mechanistic insight is that it can be put to use to remedy the condition. The proximal regulatory domain of the CTM is still present in R1827X channels (Fig. 1a). Accordingly, we tested whether we can functionally rescue the R1827X mutant by supplying the missing (distal) portion of the CTM domain. This was indeed the case: co-expression of a separate C-terminal peptide (C_{122}) that contains the distal C-terminal regulatory domain restored channel properties to mutant R1827X channels that rendered them indistinguishable from wild type Cav1.4 channels: calcium-dependent inactivation was abolished (Fig. 10c, d) and voltage-dependent activation was also shifted to the range of the wild type channel (Fig. 10e).

3. Discussion

Clinical medicine defines disease phenotypes by extracting key features from variable manifestations. These diagnostic categories are useful for the management of patients and for defining the standard of care. It is, however, clear that some of the variations in disease manifestations arise from different mutations in the individual gene and/or in the genome of the individual (giving rise to modifying genes). CSBN2 is a case in point. The clinical course is variable and there are several mutations. Here, we selected the mutation L860P. This substitution of proline for the non-conserved leucine at position 860 was also previously identified independently in two families [14,15]. Based on molecular modelling, L860P was suspected to result in destabilization of the protein. It is representative of additional mutants that are nested in the core channel folding domains (for review see ref. [22]). We selected an additional mutation R1827X that results in truncation of a functional domain that is absent in closely related channels (e.g., short Cav1.3 channels; 12) and thus unlikely to impair protein folding. Our experiments document that CSBN2 is the phenotypic manifestation of very distinct mechanistic defects.

In L860P channels, our functional data point to a loss-of-function due to a reduced number of functionally active channels expressed without

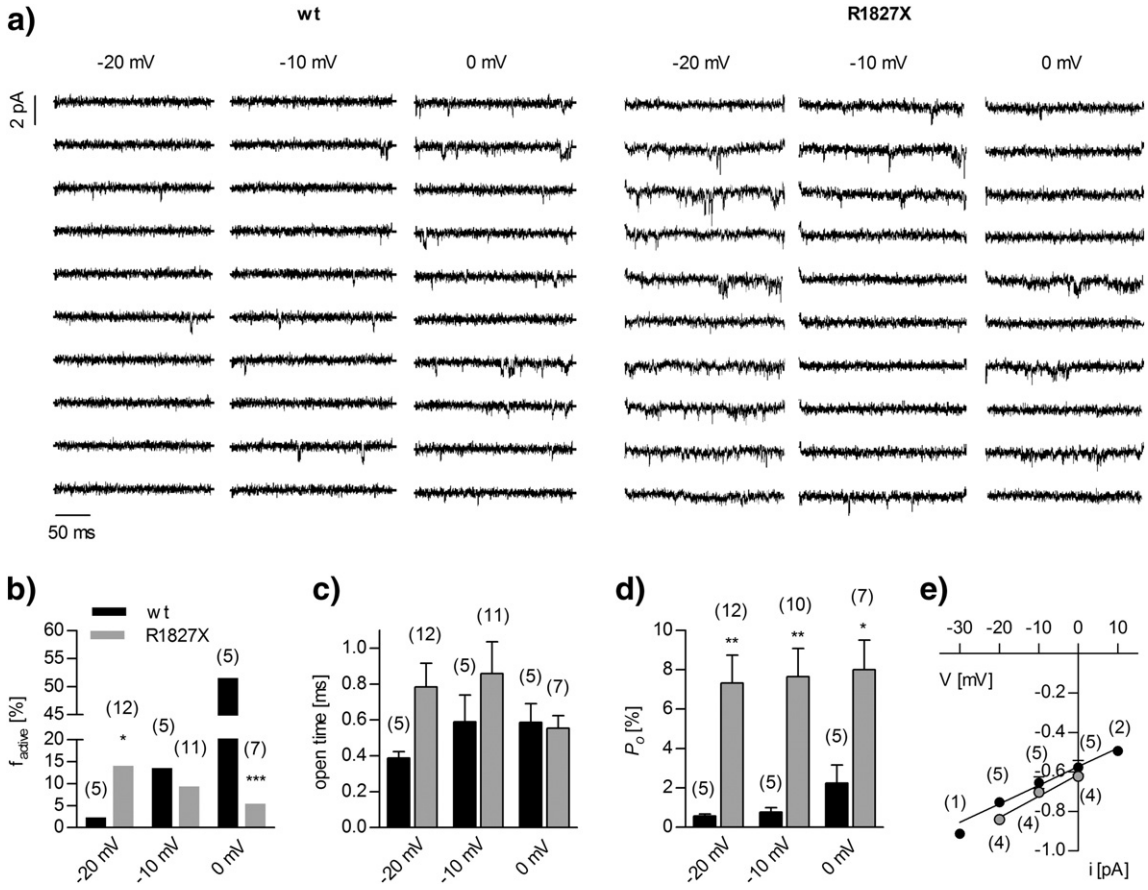

Fig. 11. Single-channel recordings obtained with either wild type or R1827X channels. (a) Exemplary consecutive traces (obtained with 110 mM Ba^{2+} as charge carrier in the presence of 10 μM BayK) show enhanced activity of R1827X channels compared to wild type (wt) at different test potentials. (b–d) Statistics on single-channel gating parameters: (b) fraction of active sweeps, (c) open times, (d) open probability (*Po*). Note that the *Po* of R1827X channels was higher at any given test potential. (e) Analysis of amplitudes obtained from well-resolved single-channel openings at different test potentials revealed similar unitary conductance of 8.9 ± 1.0 pS, n = 5 and 10.9 ± 0.5 pS, n = 4 for wild type and R1827X, respectively. *, $p < 0.05$; **, $p < 0.01$; ***, $p < 0.001$; unpaired Student's *t*-test.

gross changes of the channel gating properties, a finding that is supported by both our whole-cell and single-channel experiments. Due to a similar level of reduction of Cav1.4 activity it is tempting to ask whether the *Cacna1f*^{nob2} mouse might mimic the functional consequences of the L860P mutation for retinal transmission. ERG recordings from *Cacna1f*^{nob2} mice showed a selective b-wave defect under scotopic and photopic adaptation conditions. Retinal structures in these mice were disorganized with a substantial reduction in the thickness of the outer plexiform layer with extension of ectopic neurons to the outer nuclear layer [33]. This mouse model was initially reported to carry a natural Cav1.4 null mutation before. Doering and colleagues then demonstrated that approximately 10% of the mRNA represented a transcript in which alternative splicing removed the mutation and therefore coded for a fully functional Cav1.4 protein [32]. The present observations show that heterologously expressed wild type channels were quite stable; similar to observations were made in native tissue or (neuronal) cell lines in other voltage-gated calcium [34–36] or also sodium channels [37–39]. In case of the L860P mutation, homology modelling implied an impact on the channel stability that might result in misfolded Cav1.4 channel protein. In line with this hypothesis our CHX experiments indicated that the mutated channel is subject to increased degradation. To the best of our knowledge this is the first report showing this experimentally for a Cav1.4 mutation causing CSNB2 in patients. We have chosen the L860P mutant as one example of many CSNB2 mutations that are suggested to result in a loss-of-function due to decreased protein stability. Detailed morphological studies on a *Cacan1f*-deficient mouse model showed that loss of Cav1.4 channels causes defects in ribbon synapse formation and aberrant cone morphology, displaying also signs of cone degeneration [40–43]. Although no CSNB2 mouse models carrying potentially folding deficient Cav1.4 mutations exist so far, it's well accepted in many other inherited retinal diseases that mutations in the associated proteins cause misfolding or defective targeting [44,45]. As a general concept these processes put a burden on the protein degradation machinery and might therefore also trigger cell death.

Cav1.4 truncating mutations with impaired CTM function previously led to the discovery of a novel inhibitory feedback mechanism in LTCCs that depends on a gating modifier in the C-terminus [11–13,46]. This opened a new field of LTCC research that can use this intramolecular modulator as study tool to adjust intracellular Ca^{2+} activity. Clinical data from five patients from two families (one is reported in this study) point also to a 'hot spot' for CSNB2 mutation in the C-terminus of Cav1.4 channels. A hyperpolarizing shift in the current voltage relationship is suggested to result in a reduction of the dynamic range of the photoreceptor. We can speculate about the consequences for retinal function e.g. in the rod pathway: a reduction in the dynamic range of transmission from darkness to light would mean less depolarization of the rod bipolar cells at a given light intensity. AII amacrine cells might be activated to a lesser degree and ON ganglion cell output is expected to be decreased. AII amacrine cells also feed rod signals via inhibitory glycinergic synapses into OFF cone bipolar cells and from there to OFF ganglion cell, and therefore inhibit the OFF pathway. One might expect that this inhibition is also suppressed in mutant retinas. The interpretation of the functional phenotype in R1827X channels is complicated by the occurrence of prominent inactivation of calcium current at potentials relevant for photoreceptor signalling. However, the expected reduced calcium influx predicts a further reduction in the dynamic

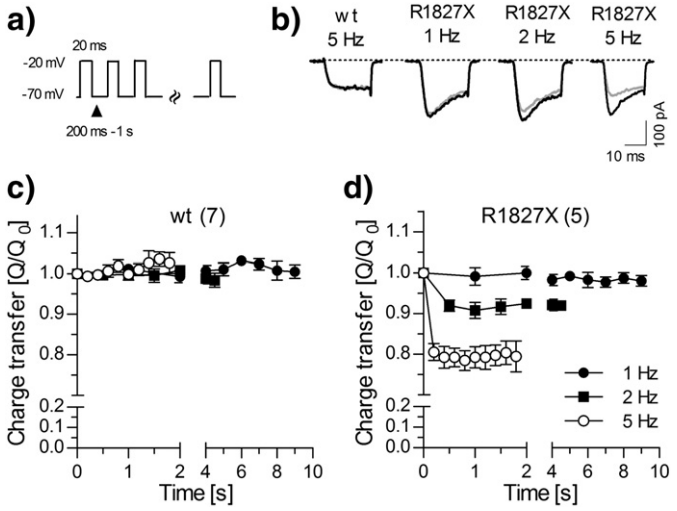

Fig. 12. Frequency-dependent inactivation of wild type and mutant R1827X channels. The experiment was performed in the presence of 15 mM Ca^{2+} and 3 μM BayK and using the following pulse protocol (a): 20 ms depolarizing pulses to −20 mV were applied at frequencies of 1, 2 and 5 Hz from a holding potential of −70 mV. (b) Representative traces for wild type (wt; cell: 13122089.abf) and R1827X (cell: 13122049-55.abf) at different frequencies are depicted in the lower panel. Black traces represent the first, grey the second pulse of the train. (c, d) Frequency-dependent changes in the charge transfer in wild type (n = 3; c) and R1827X (n = 5, d) at 1, 2 and 5 Hz. All integrated currents were normalized to the first (Q_0) 20 ms depolarizing pulse (Q/Q_0).

range of photoreceptor activity. Currently, a mouse model is not available that allows testing for these effects in isolated whole-mount retinas and/or *in vivo*.

Importantly, analyses of *in vivo* models have to take into account that the altered Ca^{2+} signalling mediated by either loss-of-function phenotype might result in changes in retinal morphology already early in development that contribute to the overall dysfunction in retinal transmission as suggested from recent studies in Cav1.4 deficient mice [42,47]. Potential pharmaco-therapeutic interventions might therefore have to be applied early in development. Gene therapeutic approaches focus on recombinant viral vectors as promising vehicles for therapeutic gene delivery to the retina (for review see e.g. [48,49]). Gene therapy may be applicable in patients carrying the R1827X mutation. This conjecture is supported by our rescue experiment. It is also conceivable that patients with a mutation phenotypically related to the L860P may benefit from gene therapy. It is, however, worthwhile to consider an alternative approach, i.e., pharmacochaperoning by using ligands that stabilize folding intermediates in the endoplasmic reticulum and thus prevent ER-associated degradation. Understanding the folding trajectory of Cav1.4 will be helpful in the search for ligands that act as pharmacochaperones. In the meantime, it is worth noting that valproic acid has been suggested to act as pharmacological chaperone for unfolded proteins and is being explored in an ongoing clinical trial in patients with autosomal dominant retinitis pigmentosa (http://clinicaltrials.gov/ct2/show/study/NCT01233609).

Supplementary data to this article can be found online at http://dx.doi.org/10.1016/j.bbamem.2014.04.023.

Acknowledgements

We thank Dagmar Knoflach for the excellent technical support and Sakine Korkmaz for assistance with the Western Blot analyses. We also thank Walter Sandtner for the discussions on gating current analysis, and Stefan Münkner, Jutta Engel and Tobias Moser for their valuable input and discussion on NSNA experiments.

References

[1] J. Striessnig, H.J. Bolz, A. Koschak, Pflugers Arch. 460 (2010) 361–374.
[2] R. Jalkanen, N.T. Bech-Hansen, R. Tobias, E.M. Sankila, M. Mantyjarvi, H. Forsius, A. de la Chapelle, T. Alitalo, Invest. Ophthalmol. Vis. Sci. 48 (2007) 2498–2502.
[3] R. Jalkanen, M. Mantyjarvi, R. Tobias, J. Isosomppi, E.M. Sankila, T. Alitalo, N.T. Bech-Hansen, J. Med. Genet. 43 (2006) 699–704.
[4] C.I. Hope, D.M. Sharp, A. Hemara-Wahanui, J.I. Sissingh, P. Lundon, E.A. Mitchell, M.A. Maw, G.M. Clover, Clin. Exp. Ophthalmol. 33 (2005) 129–136.
[5] H.J. Simonsz, R.J. Florijn, H.M. van Minderhout, A.A. Bergen, M. Kamermans, Strabismus 17 (2009) 158–164.
[6] N.T. Bech-Hansen, M.J. Naylor, T.A. Maybaum, W.G. Pearce, B. Koop, G.A. Fishman, M. Mets, M.A. Musarella, K.M. Boycott, Nat. Genet. 19 (1998) 264–267.
[7] K.M. Boycott, W.G. Pearce, M.A. Musarella, R.G. Weleber, T.A. Maybaum, D.G. Birch, Y. Miyake, R.S. Young, N.T. Bech-Hansen, Am. J. Hum. Genet. 62 (1998) 865–875.
[8] G. Schubert, H. Bornschein, Ophthalmologica 123 (1952) 396–413.
[9] Y. Miyake, K. Yagasaki, M. Horiguchi, Y. Kawase, T. Kanda, Arch. Ophthalmol. 104 (1986) 1013–1020.
[10] A. Singh, D. Hamedinger, J.C. Hoda, M. Gebhart, A. Koschak, C. Romanin, J. Striessnig, Nat. Neurosci. 9 (2006) 1108–1116.
[11] C. Wahl-Schott, L. Baumann, H. Cuny, C. Eckert, K. Griessmeier, M. Biel, Proc. Natl. Acad. Sci. U. S. A. 103 (2006) 15657–15662.
[12] G. Bock, M. Gebhart, A. Scharinger, W. Jangsangthong, P. Busquet, C. Poggiani, S. Sartori, M.E. Mangoni, M.J. Sinnegger-Brauns, S. Herzig, J. Striessnig, A. Koschak, J. Biol. Chem. 286 (2011) 42736–42748.
[13] J.T. Hulme, K. Konoki, T.W. Lin, M.A. Gritsenko, D.G. Camp II, D.J. Bigelow, W.A. Catterall, Proc. Natl. Acad. Sci. U. S. A. 102 (2005) 5274–5279.
[14] T.M. Strom, G. Nyakatura, E. Apfelstedt-Sylla, H. Hellebrand, B. Lorenz, B.H. Weber, K. Wutz, N. Gutwillinger, K. Ruther, B. Drescher, C. Sauer, E. Zrenner, T. Meitinger, A. Rosenthal, A. Meindl, Nat. Genet. 19 (1998) 260–263.
[15] K. Wutz, C. Sauer, E. Zrenner, B. Lorenz, T. Alitalo, M. Broghammer, M. Hergersberg, A. de la Chapelle, B.H. Weber, B. Wissinger, A. Meindl, C.M. Pusch, Eur. J. Hum. Genet. 10 (2002) 449–456.
[16] J.C. Hoda, F. Zaghetto, A. Koschak, J. Striessnig, J. Neurosci. 25 (2005) 252–259.
[17] S.M. Baig, A. Koschak, A. Lieb, M. Gebhart, C. Dafinger, G. Nurnberg, A. Ali, I. Ahmad, M.J. Sinnegger-Brauns, N. Brandt, J. Engel, M.E. Mangoni, M. Farooq, H.U. Khan, P. Nurnberg, J. Striessnig, H.J. Bolz, Nat. Neurosci. 14 (2011) 77–84.
[18] I. Romero-Calvo, B. Ocon, P. Martinez-Moya, M.D. Suarez, A. Zarzuelo, O. Martinez-Augustin, F.S. de Medina, Anal. Biochem. 401 (2010) 318–320.
[19] O. Alvarez, C. Gonzalez, R. Latorre, Adv. Physiol. Educ. 26 (2002) 327–341.
[20] T. Stockner, A. Koschak, Biochim. Biophys. Acta 1828 (2013) 1598–1607.
[21] R.C. Edgar, BMC Bioinforma. 5 (2004) 113.
[22] J. Payandeh, T. Scheuer, N. Zheng, W.A. Catterall, Nature 475 (2011) 353–358.
[23] M.A. Marti-Renom, R.H. Stote, E. Querol, F.X. Aviles, M. Karplus, Proteins 40 (2000) 482–493.
[24] A. Sali, J.P. Overington, Protein Sci. 3 (1994) 1582–1596.
[25] M.Y. Shen, A. Sali, Protein Sci. 15 (2006) 2507–2524.
[26] F. Bezanilla, Physiol. Rev. 80 (2000) 555–592.
[27] C.J. Doering, J. Hamid, B. Simms, J.E. McRory, G.W. Zamponi, Biophys. J. 89 (2005) 3042–3048.
[28] T. Schneider-Poetsch, J. Ju, D.E. Eyler, Y. Dang, S. Bhat, W.C. Merrick, R. Green, B. Shen, J.O. Liu, Nat. Chem. Biol. 6 (2010) 209–217.
[29] B. Belles, C.O. Malecot, J. Hescheler, W. Trautwein, Pflugers Arch. 411 (1988) 353–360.
[30] D. Knoflach, V. Kerov, S.B. Sartori, G.J. Obermair, C. Schmuckermair, X. Liu, V. Sothilingam, M.G. Garrido, S.A. Baker, M. Glosmann, K. Schicker, M. Seeliger, A. Lee, A. Koschak, Channels (Austin) 7 (2013).
[31] J. An, L. Wang, Q. Guo, L. Li, F. Xia, Z. Zhang, J. Neurogenet. 26 (2012) 363–373.
[32] V. Yarotskyy, G. Gao, B.Z. Peterson, K.S. Elmslie, J. Physiol. 587 (2009) 551–565.
[33] B. Chang, J.R. Heckenlively, P.R. Bayley, N.C. Brecha, M.T. Davisson, N.L. Hawes, A.A. Hirano, R.E. Hurd, A. Ikeda, B.A. Johnson, M.A. McCall, C.W. Morgans, S. Nusinowitz, N.S. Peachey, D.S. Rice, K.A. Vessey, R.G. Gregg, Vis. Neurosci. 23 (2006) 11–24.
[34] X. Yang, G. Chen, R. Papp, D.B. Defranco, F. Zeng, G. Salama, J. Physiol. 590 (2012) 493–508.
[35] R.N. Leach, J.C. Desai, C.H. Orchard, Cell Calcium 38 (2005) 515–526.
[36] M. Passafaro, F. Clementi, E. Sher, J. Neurosci. 12 (1992) 3372–3379.
[37] C.J. Waechter, J.W. Schmidt, W.A. Catterall, J. Biol. Chem. 258 (1983) 5117–5123.
[38] E. Monjaraz, A. Navarrete, L.F. Lopez-Santiago, A.V. Vega, J.A. Arias-Montano, G. Cota, J. Physiol. 523 (Pt 1) (2000) 45–55.
[39] N. Storey, D. Latchman, S. Bevan, J. Cell Biol. 158 (2002) 1251–1262.
[40] D. Specht, S.B. Wu, P. Turner, P. Dearden, F. Koentgen, U. Wolfrum, M. Maw, J.H. Brandstatter, S. tom Dieck, Invest. Ophthalmol. Vis. Sci. 50 (2009) 505–515.
[41] S. Michalakis, K. Schaferhoff, I. Spiwoks-Becker, N. Zabouri, S. Koch, F. Koch, M. Bonin, M. Biel, S. Haverkamp, Cell. Mol. Life Sci. 70 (2013) 1831–1847.
[42] N. Zabouri, S. Haverkamp, PLoS One 8 (2013) e63853.
[43] X. Liu, V. Kerov, F. Haeseleer, A. Majumder, N. Artemyev, S.A. Baker, A. Lee, Channels (Austin) (2013) 7.
[44] R. Tzekov, L. Stein, S. Kaushal, Cold Spring Harb. Perspect. Biol. 3 (2011) a007492.
[45] D. Athanasiou, M. Aguila, D. Bevilacqua, S.S. Novoselov, D.A. Parfitt, M.E. Cheetham, FEBS Lett. 587 (2013) 2008–2017.

[46] A. Singh, M. Gebhart, R. Fritsch, M.J. Sinnegger-Brauns, C. Poggiani, J.C. Hoda, J. Engel, C. Romanin, J. Striessnig, A. Koschak, J. Biol. Chem. 283 (30) (2008) 20733–20744.
[47] M.A. Raven, N.C. Orton, H. Nassar, G.A. Williams, W.K. Stell, G.H. Jacobs, N.T. Bech-Hansen, B.E. Reese, J. Comp. Neurol. 506 (2008) 745–758.
[48] S.E. Boye, S.L. Boye, A.S. Lewin, W.W. Hauswirth, Mol. Ther. 21 (2013) 509–519.
[49] D.M. Lipinski, M. Thake, R.E. MacLaren, Prog. Retin. Eye Res. 32 (2013) 22–47.